Scale dependence of the alignment between strain rate and rotation in turbulent shear flow

D. Fiscaletti,[1,2,*] G. E. Elsinga,[1] A. Attili,[3,4] F. Bisetti,[3,5] and O. R. H. Buxton[6]

[1]*Laboratory for Aero and Hydrodynamics, Department of Mechanical, Maritime, and Materials Engineering, Delft University of Technology, The Netherlands*

[2]*Engineering and the Environment, University of Southampton, Southampton SO17 1BJ, United Kingdom*

[3]*Clean Combustion Research Center, King Abdullah University of Science and Technology, Thuwal 23955-6900, Saudi Arabia*

[4]*Institute for Combustion Technology, RWTH Aachen University, 52056 Aachen, Germany*

[5]*Department of Aerospace Engineering and Engineering Mechanics, University of Texas at Austin, Austin, Texas 78712-1085, USA*

[6]*Department of Aeronautics, Imperial College London, London SW7 2AZ, United Kingdom*

(Received 18 April 2016; published 24 October 2016)

The scale dependence of the statistical alignment tendencies of the eigenvectors of the strain-rate tensor $\boldsymbol{e}_i$, with the vorticity vector $\boldsymbol{\omega}$, is examined in the self-preserving region of a planar turbulent mixing layer. Data from a direct numerical simulation are filtered at various length scales and the probability density functions of the magnitude of the alignment cosines between the two unit vectors $|\boldsymbol{e}_i \cdot \hat{\boldsymbol{\omega}}|$ are examined. It is observed that the alignment tendencies are insensitive to the concurrent large-scale velocity fluctuations, but are quantitatively affected by the nature of the concurrent large-scale velocity-gradient fluctuations. It is confirmed that the small-scale (local) vorticity vector is preferentially aligned in parallel with the large-scale (background) extensive strain-rate eigenvector $\boldsymbol{e}_1$, in contrast to the global tendency for $\boldsymbol{\omega}$ to be aligned in parallel with the intermediate strain-rate eigenvector [Hamlington *et al.*, Phys. Fluids **20**, 111703 (2008)]. When only data from regions of the flow that exhibit strong swirling are included, the so-called high-enstrophy worms, the alignment tendencies are exaggerated with respect to the global picture. These findings support the notion that the production of enstrophy, responsible for a net cascade of turbulent kinetic energy from large scales to small scales, is driven by vorticity stretching due to the preferential parallel alignment between $\boldsymbol{\omega}$ and nonlocal $\boldsymbol{e}_1$ and that the strongly swirling worms are kinematically significant to this process.

DOI: 10.1103/PhysRevFluids.1.064405

I. INTRODUCTION

In the Richardson-Kolmogorov picture of turbulent flow, the turbulent kinetic energy contained at large scales cascades, via inertial processes, to increasingly small spatial scales until this energy may ultimately be dissipated into internal energy by viscous processes [1,2]. Note that this cascade is a mean picture and backscatter, in which energy is transferred from small to large scales, is almost as likely as forward scatter [3]. The separation (in spatial wave-number space) between these large scales and the smallest, dissipative scales is determined by the Reynolds number Re with an increasing separation as Re increases. The Kolmogorov theories [2,4], which are formulated for high-Reynolds-number flows and thus a large spectral separation between the large and small scales, assume that the smallest scales are statistically isotropic. For turbulent shear flows, the large scales are anisotropic [5] and thus directionality is assumed to be lost through the cascade of turbulent kinetic energy (TKE). However, Batchelor and Townsend [6] postulated that TKE may in fact be transferred directly to the small scales without the involvement of the intermediate, inertial range of

*Corresponding author: d.fiscaletti@tudelft.nl

scales. More recently, Yeung *et al.* [7] showed that this transfer of TKE from large to small scales can indeed be a single-step process. Evidence in support of this argument was provided by Shen and Warhaft [8], who showed that even at very large Reynolds numbers the small-scale structure is anisotropic, with the highest-order moments increasing with the Reynolds number. According to this observation, the explanation of directionality as a consequence of the moderate Reynolds number of the flow, in which the separation in the wave-number space between the large and small scales is not sufficiently large, is less credible.

The prospect of a single-step transfer of TKE opens the possibility that the anisotropy of the large scales may not be completely lost, leading to an interaction between the large and small scales present in the flow. The work of Bandyopadhyay and Hussain [9] was among the first studies to show the interaction between large and small scales in turbulent flows, both wall-bounded and boundary-free shear flows. By examining the short-time correlations between the low-pass-filtered velocity fluctuations (from hot-wire experiments) and the envelope of the high-pass-filtered (small-scale) signal the authors were able to demonstrate a significant degree of coupling for all shear flows. Since this pioneering work, a significant amount of research has focused on the interaction between the large, outer scales and the small, near-wall scales of wall-bounded turbulent flows. Nevertheless, some significant progress has been made examining these scale interactions in free shear flows by drawing an analogy between subgrid-scale (SGS) models from large-eddy simulations, which account for the flux of energy from the large, resolved scales to the small scales in such simulations. Meneveau [10], for example, computed the joint moments between experimentally measured SGS stresses and the corresponding large-scale (filtered) velocity fluctuations in grid turbulence. Similar measurements were performed by Buxton and Ganapathisubramani [11] in which planar velocity fields were simultaneously measured at two separate spatial resolutions such that statistical moments of the SGS stresses could be conditioned on the concurrent large-scale velocity fluctuations in a turbulent mixing layer. It was shown that close to the geometric centerline, but slightly to the high-speed side of the mixing layer, negative large-scale velocity fluctuations were situated concurrently to enhanced small-scale activity. Later, Buxton [12] observed for the correlation between the SGS stresses and the concurrent large-scale velocity fluctuation in the low-speed side of the mixing layer behavior opposite to that on the high-speed side, i.e., enhanced small-scale activity concurrent with positive large-scale velocity fluctuations. Further, in agreement with O'Neil and Meneveau [13], it was shown that the large-scale velocity fluctuations impact the statistical distribution of the small-scale velocity gradient phenomena.

Buxton [12] showed that positive large-scale velocity fluctuations (on the low-speed side of a mixing layer) are collocated with increased small-scale dissipation ϵ and enstrophy ω^2 ($\boldsymbol{\omega} = \boldsymbol{\nabla} \times \boldsymbol{u}$ is the vorticity vector). This behavior was confirmed by Fiscaletti *et al.* [14]. However, Fiscaletti *et al.* [14] further showed that the correlation between the large-scale velocity fluctuations and the small-scale enstrophy is well approximated by a product of two correlation functions $R_{uA} \approx R_{ug} R_{gA}$. In this relationship, R_{ug} is the correlation coefficient between the large-scale velocity fluctuation and the authors' metric for the magnitude of the large-scale velocity gradients and R_{gA} is the correlation coefficient between the large-scale velocity gradients and the small-scale enstrophy. It was observed that R_{ug} exhibited the same crosswise (y) dependence as R_{uA}, with a negative correlation on the high-speed side of the mixing layer and a positive correlation on the low-speed side of the mixing layer, whereas R_{gA} exhibited a near constant value, close to unity, throughout the mixing layer. The authors thus argued that this scale interaction was primarily driven by the large-scale velocity-gradient fluctuations, as opposed to the large-scale velocity fluctuations.

Whether by a single-step process, as observed by Yeung *et al.* [7], or through an accelerated cascade due to the minimal size of the inertial range of scales in moderate-Reynolds-number turbulence, the only known way in which energy is inertially transferred from large to small scales is through vorticity stretching. The vorticity stretching term $\omega_i s_{ij} \omega_j$ may be either positive or negative, but Taylor [15] was the first to observe that the ensemble average $\langle \omega_i s_{ij} \omega_j \rangle > 0$, i.e., vorticity stretching, is favored over vorticity compression, which fits with the Richardson-Kolmogorov picture of the turbulent cascade. Betchov [16] showed that this term may be written as

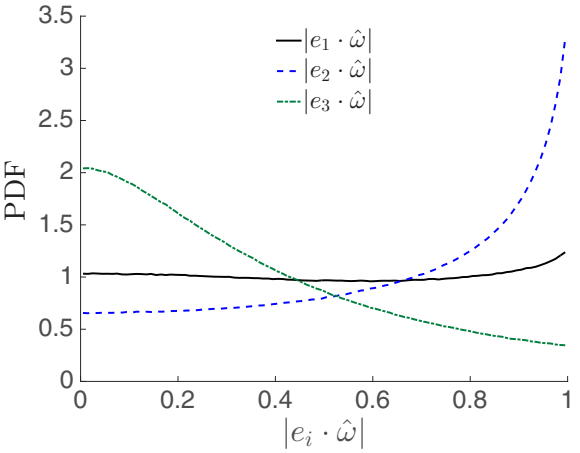

FIG. 1. Probability density functions of the magnitude of the alignment between the strain-rate eigenvectors and the vorticity vector in the fully developed region of a turbulent mixing layer, at a Reynolds number based on the Taylor microscale of $\mathrm{Re}_\lambda = 250$. The data set used to produce this figure is obtained from Attili and Bisetti [23] and it is the object of the analysis reported in the present article (a description is given in Sec. II).

$\omega_i s_{ij} \omega_j = \omega^2 s_i (\boldsymbol{e}_i \cdot \hat{\boldsymbol{\omega}})^2$, in which summation over index i is implicit, s_i are the eigenvalues of the strain-rate tensor $s_{ij} = (\partial u_i'/\partial x_j + \partial u_j'/\partial x_i)/2$, with corresponding unit eigenvectors $\boldsymbol{e}_i$, and $\hat{\boldsymbol{\omega}}$ is the unit vector indicating the direction of the vorticity vector. The vorticity stretching term may thus be observed as the manifestation of the interaction between strain rate and rotation and is also susceptible to scale interactions within a turbulent flow [17,18].

Consideration of the form of $\omega_i s_{ij} \omega_j$ proposed by Betchov [16] suggests that such scale interactions may be due to amplification and attenuation of the small-scale enstrophy–strain-rate eigenvalue products, a modification of the vector alignment tendencies between the small-scale vorticity vector and eigenframe of s_{ij}, or the correlation between the two. The amplification and attenuation of ω^2 and $s_{ij} s_{ij}$ by concurrent large-scale velocity fluctuations has already been shown by Buxton [12] and by Fiscaletti *et al.* [14]. In addition, Fiscaletti *et al.* [14] found that the large-scale velocity gradients amplify ω^2 almost linearly. The motivation for the current work is thus to assess the scale dependence of the alignment tendencies between $\boldsymbol{\omega}$ and $\boldsymbol{e}_i$. The eigenvalues s_i may be ordered such that $s_1 \geqslant s_2 \geqslant s_3$, with $s_1 \geqslant 0$ (extensive strain rate), $s_3 \leqslant 0$ (compressive strain rate), and continuity for an incompressible flow demanding that $\sum_{i=1}^{3} s_i = 0$. There is overwhelming evidence in the literature that the vorticity vector preferentially aligns parallel to the intermediate eigenvector $\boldsymbol{e}_2$ and perpendicularly to the compressive eigenvector with no preferential alignment tendency to the extensive eigenvector [19–22]. The probability density functions (PDFs) for the magnitude of these alignments are presented in Fig. 1 from the mixing layer flow at $\mathrm{Re}_\lambda = 250$, which is the object of the analysis of this article (more detail on the flow is given in Sec. II). However, Buxton and Ganapathisubramani [24] observed that the alignment preference between $\boldsymbol{\omega}$ and $\boldsymbol{e}_1$ determines the sign of $\omega_i s_{ij} \omega_j$, with parallel alignment favored for concurrent $\omega_i s_{ij} \omega_j > 0$ and perpendicular alignment favored for $\omega_i s_{ij} \omega_j < 0$. Subsequently, the commonly reported tendency for $|\boldsymbol{e}_2 \cdot \hat{\boldsymbol{\omega}}| \approx 1$ has been explained by the preferential alignment between the vorticity vector and the local intermediate strain-rate eigenvector, particularly in regions of high enstrophy [25], while $\boldsymbol{\omega}$ preferentially aligns with the extensive eigenvector of the background strain field [26]. The preferential alignment of the vorticity vector, filtered at a length scale of the characteristic diameter of the high-enstrophy worms [27–29], with the large-scale extensive strain-rate eigenvector has been confirmed by Leung *et al.* [30]. These findings go some way to linking the rotation–strain-rate alignment tendencies to the mean cascade of TKE from large scales (responsible for inducing the background strain field) to small scales. In this paper we will examine these alignments conditioned

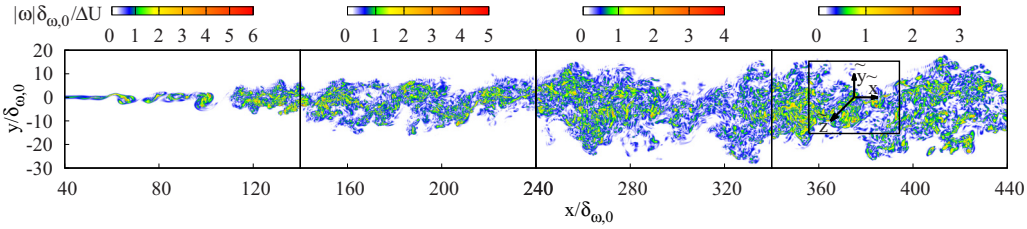

FIG. 2. Two-dimensional cut of the nondimensional vorticity magnitude field in the turbulent mixing layer. The color scale is different in the four subfigures to take into account that vorticity decreases in the streamwise direction. The black box in the rightmost subfigure identifies the region analyzed in the present study. A coordinate system $(\tilde{x},\tilde{y},\tilde{z})$ centered in $(x = 375\delta_{\omega,0}, y = 0, z = 0)$ is introduced here, which represents the frame of reference related to the region under analysis.

on the concurrent large-scale velocity and velocity-gradient fluctuations, with varying definitions for large scales. The analysis is conducted in the developed region of a planar turbulent mixing layer.

II. NUMERICAL METHODS AND CONFIGURATION

The mixing layer simulation described in the present work was performed using the parallel flow solver NGA [23,31,32]. A detailed description of the configuration and flow parameters are provided in a number of previous works [14,23,33,34] and only a brief summary is presented here.

The code solves the unsteady, incompressible Navier-Stokes equations on a spatially and temporally staggered grid with the semi-implicit fractional-step method of Kim and Moin [35]. Velocity spatial derivatives are discretized with a second-order finite-difference-centered scheme.

The flow at the inlet ($x = 0$) is a hyperbolic tangent profile for the streamwise velocity U with prescribed vorticity thickness $\delta_{\omega,0}$: $U(x = 0, y, z) = U_C + 1/2\Delta U \tanh(2y/\delta_{\omega,0})$, where $U_C = (U_1 + U_2)/2$ is the convective velocity, U_1 and U_2 are the high- and low-speed stream velocities, and $\Delta U = U_1 - U_2$ is the velocity difference across the layer. The ratio of the two velocities is $U_1/U_2 = 3$. Low-amplitude white noise is superimposed on the hyperbolic tangent profile, resulting in the onset of the Kelvin-Helmholtz instability at a short distance downstream of the inlet ($x \approx 50\delta_{\omega,0}$). The crosswise and spanwise velocity components are perturbed in the same manner. The boundary conditions are periodic in the spanwise direction z and free slip in the crosswise direction y. Free convective outflow [36] is specified at $x = L_x$.

The computational domain extends over $L_x = 473\delta_{\omega,0}$, $L_y = 290\delta_{\omega,0}$, and $L_z = 157.5\delta_{\omega,0}$ in the streamwise (x), crosswise (y), and spanwise (z) directions, respectively. The domain is discretized with $3072 \times 940 \times 1024 \approx 3 \times 10^9$ grid points ($N_x \times N_y \times N_z$). In the region centered around $y = 0$ ($|y| \leqslant 45\delta_{\omega,0}$), the grid is homogeneous in the three directions: $\Delta x = \Delta y = \Delta z = 0.15\delta_{\omega,0}$. Outside the core region for $|y| > 45\delta_{\omega,0}$, the grid is stretched linearly until $\Delta y = 0.6\delta_{\omega,0}$ at $|y| = 55\delta_{\omega,0}$ and then is constant again up to the boundary. Overall, the spatial resolution is such that $\Delta x = \Delta y = \Delta z \leqslant 2.5\eta$ everywhere, where $\eta = \nu^{3/4}\varepsilon^{-1/4}$ is the Kolmogorov scale and ε the average turbulent kinetic energy dissipation. The time step size is calculated in order to have a unity Courant-Friedrichs-Lewy number.

Figure 2 shows an overview of the spatially developing mixing layer. The present analysis is performed in the fully developed region, where the flow achieves a Reynolds number based on the Taylor microscale $\mathrm{Re}_\lambda = 250$, calculated with the formula 2.14 of Pantano and Sarkar [37]. Twenty-one three-dimensional subdomains of size $16.7\lambda \times 13.3\lambda \times 68.3\lambda$ ($\lambda \approx 30\eta$ is the Taylor microscale), collected at different time instants, were considered in the analysis. The Taylor microscale λ is obtained as [38]

$$\lambda = u_{\mathrm{rms}}\sqrt{\frac{15\nu}{\epsilon}}.$$

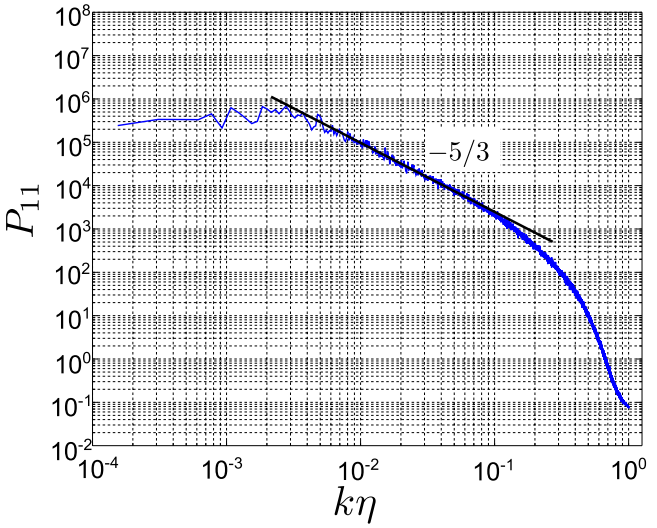

FIG. 3. Velocity power spectrum from a time series obtained from the DNS mixing layer object of the present analysis, at the crosswise position $\tilde{y} = -2.06$ and $\tilde{x} = \tilde{z} = 0$.

The center of these subdomains is located at a streamwise position $x = 375\delta_{\omega,0}$ and $y = 0$. The convective distance between two consecutive subdomains, computed after applying the Taylor hypotheses, is $167\delta_{\omega,0}$, corresponding to 68 Taylor microscales and 2000 Kolmogorov scales approximately; therefore, the subdomains are statistically independent. The subdomains span the entire length of the simulation domain in the spanwise direction z. It is worth mentioning that the subdomains might contain bulges of potential flow. Figure 5(c) of Ref. [34] shows the average crosswise location of the turbulent-nonturbulent (TNT) interface, at different streamwise positions. While the average turbulent-nonturbulent interface on the high-speed side of the mixing layer approximately matches the upper edge of the subdomains examined in the present study, the average TNT interface on the low-speed side of the flow is largely external to the lower edge of these subdomains. This can be appreciated also in Fig. 5(a) of Ref. [34]. Therefore, the subdomains are located within the average turbulent-nonturbulent interfaces and the flow is predominantly turbulent. Therefore, the presence of entrained potential flow can be considered irrelevant to the statistics computed in the following.

As shown in Fig. 2, a coordinate system $(\tilde{x},\tilde{y},\tilde{z})$ centered at $x = 375\delta_{\omega,0}$, $y = 0$, and $z = 0$ and nondimensionalized by the Taylor length scale λ is introduced. The coordinate system is oriented so that positive values of $\tilde{y}$ are on the high-velocity side of the mixing layer. Figure 3 shows the velocity power spectrum obtained from a time series converted into a space series with the Taylor hypothesis [39], at $\tilde{x} = 0$, $\tilde{y} = -2.06$, and $\tilde{z} = 0$. The inertial subrange, characterized by the typical $-5/3$ slope and highlighted in the figure, spans over more than one and a half decades. This is evidence of the turbulent nature of the flow and shows that there is a clear separation between the large and the small scales of turbulence.

III. SEPARATION OF SCALES AND FILTERING PROCEDURES

The primary goal of the paper is to study the alignment between the vorticity vector and the eigenvectors of the strain-rate tensor at different scales. The different scales of turbulence were obtained by directly filtering the data in physical space. This means that we did not apply the Taylor hypothesis of frozen turbulence, which is normally used to convert time series into spatial signals.

This section illustrates the filtering procedure to calculate the large-scale quantities that are used in Sec. IV.

Moving average filters with a cube side of one Taylor length scale ($\Lambda = \lambda$), two Taylor length scales ($\Lambda = 2\lambda$), and three Taylor length scales ($\Lambda = 3\lambda$) were applied to the 21 three-dimensional (3D) velocity vector fields, with Λ denoting the filter size throughout the article. From this procedure, the 3D filtered velocity fields U_L, V_L, and W_L were obtained. The spectral leakage associated with the moving average filtering was assessed by comparison with a Gaussian filter (characterized by the same cube size and by a standard deviation of 0.65 the cube size) and it was found to be negligible for the aim of the present analysis. The 3D filtered velocity fields permitted the calculation of $\tilde{s}_{ij}$ and $\tilde{\boldsymbol{\omega}}$, which denote the filtered strain-rate tensor and the filtered vorticity vector, respectively.

As a secondary aim of the study, the alignment between the vorticity vector and the eigenvectors of the strain-rate tensor was conditioned on large-scale velocity and velocity-gradient fluctuations. The local strength of these large-scale signals was calculated as follows. At a given crosswise position $\tilde{y}$, a number of different signals representative of the large scales were created, considering both large-scale velocity fluctuations $u_L(\tilde{x},\tilde{y},\tilde{z},t)$ and large-scale velocity gradients $g_L(\tilde{x},\tilde{y},\tilde{z},t)$. The large-scale velocity signal is simply $u_L(\tilde{x},\tilde{y},\tilde{z},t) = U_L(\tilde{x},\tilde{y},\tilde{z},t) - U_m(\tilde{y})$, where U_L is the filtered velocity field with $\Lambda = \lambda$ and $U_m(\tilde{y})$ is the ensemble-average streamwise velocity at $\tilde{y}$. The large-scale velocity fluctuations were nondimensionalized by the velocity difference over the mixing layer ΔU, therefore $u_L^*(\tilde{x},\tilde{y},\tilde{z},t) = u_L(\tilde{x},\tilde{y},\tilde{z},t)/\Delta U$. The local large-scale gradient signal $g_L(\tilde{x},\tilde{y},\tilde{z},t)$, computed in a $(\lambda)^3$-sized cube centered on $(\tilde{x},\tilde{y},\tilde{z})$, at time t, was calculated using the following relationship, which includes only the derivatives associated with shear:

$$g_L(\tilde{x},\tilde{y},\tilde{z},t) = \frac{1}{N}\sum_{i=1}^{N}\sqrt{\left(\left|\frac{dU_L}{d\tilde{y}}\right|_i^2 + \left|\frac{dU_L}{d\tilde{z}}\right|_i^2 + \left|\frac{dV_L}{d\tilde{x}}\right|_i^2 + \left|\frac{dV_L}{d\tilde{z}}\right|_i^2 + \left|\frac{dW_L}{d\tilde{x}}\right|_i^2 + \left|\frac{dW_L}{d\tilde{y}}\right|_i^2\right)}. \tag{1}$$

The derivatives were computed with a central-difference scheme from the discrete data set in each point of the cube and averaged over the number of mesh points inside each cube N. Only the shear components of the gradients have been included in $g_L(\tilde{x},\tilde{y},\tilde{z},t)$ [Eq. (1)], since in the work by Fiscaletti *et al.* [14] the acceleration terms were found not important in the interaction between large and small scales. The large-scale velocity gradients $g_L(\tilde{x},\tilde{y},\tilde{z},t)$ at the crosswise position $\tilde{y}$ are nondimensionalized by the average of the large-scale gradients at $\tilde{y}$, $\overline{g}_L(\tilde{y})$, thus obtaining $g_L^* = g_L/\overline{g}_L$. More details on this procedure can be found in Ref. [14]. In the construction of the large-scale signals, the appropriate length scale for large-scale filtering was considered to be the Taylor microscale (and larger length scales). This is justified by the fact that the dissipation spectrum has a peak at a length scale close to the Taylor length scale, meaning that the length scales larger than the Taylor length scale contribute progressively less to dissipation and can be considered large scales. In Sec. IV the alignment between the vorticity and the eigenvectors of the strain-rate tensor is conditioned on both the large-scale velocity fluctuations $u_L^*(\tilde{x},\tilde{y},\tilde{z},t)$ and the large-scale gradients $g_L^*(\tilde{x},\tilde{y},\tilde{z},t)$.

IV. RESULTS AND DISCUSSION

The picture of the cascade of TKE described by Leung *et al.* [30] is based upon the vorticity stretching term being largely fed by the alignment of the small-scale (local) vorticity vector with the extensive strain rate of the large-scale (or background in the terminology of Hamlington *et al.* [26]) strain field. Regions for which this alignment is $|\boldsymbol{e}_1 \cdot \hat{\boldsymbol{\omega}}| \gtrsim 0.8$ provide the majority of the overall positive contribution to $\omega_i s_{ij} \omega_j$ and are thus responsible for the transfer of turbulent kinetic energy from large scales to smaller ones [30]. However, it has been shown that regions of intense enstrophy production are often collocated with the regions of strong swirling [24]. Zhou *et al.* [40] noted that the solution to the characteristic equation to calculate the eigenvalues of the velocity gradient tensor itself, $d_{ij} = \partial u_i'/\partial x_j$, may admit only three real eigenvalues or one real eigenvalue and a complex

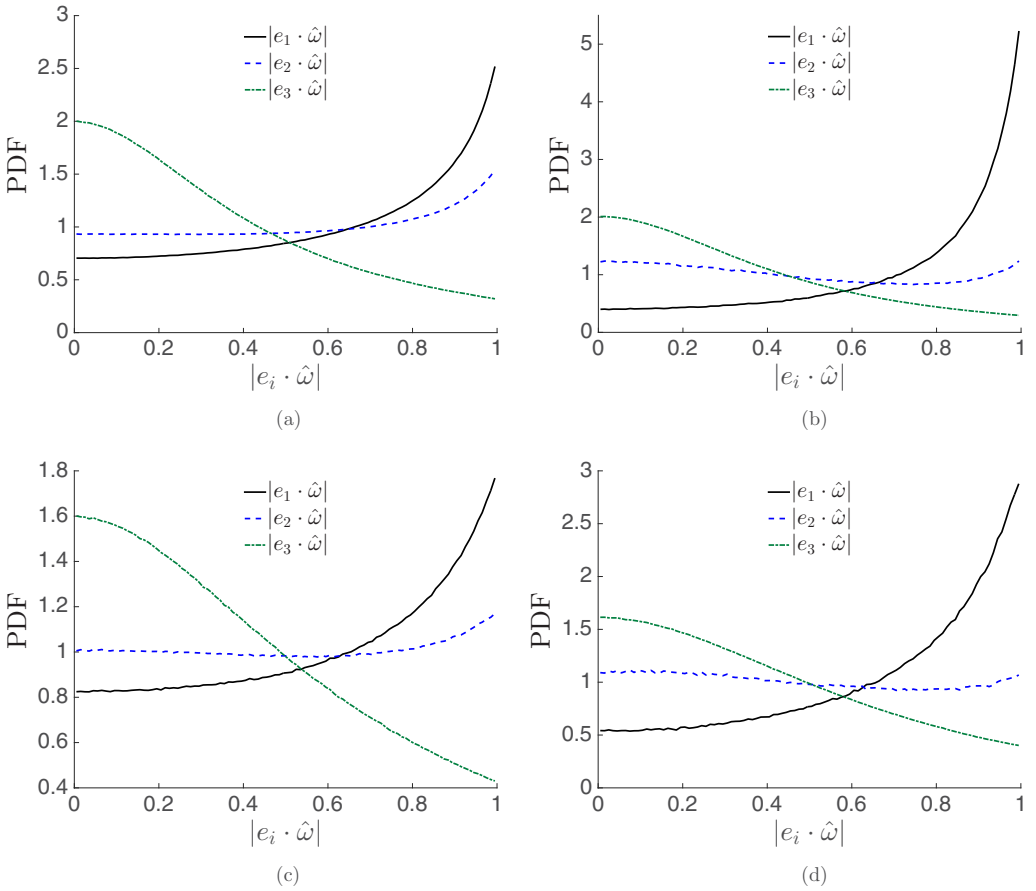

FIG. 4. Probability density functions of the alignment between the unfiltered vorticity vector and the eigenframe of the filtered strain-rate tensor. The strain-rate tensor is computed from the filtered velocity field with filter length scale (a) and (b) $\Lambda = \lambda$ and (c) and (d) $\Lambda = 3\lambda$. Data are included (a) and (c) from the entire field and (b) and (d) only from regions of intense swirling $\lambda_{ci} > 3.5\langle\lambda_{ci}\rangle$.

conjugate pair $\lambda_{cr} \pm i\lambda_{ci}$. In the latter case the real eigenvector defines an axis of swirling, with the relative strength of the local swirling quantified by λ_{ci}. Regions of intense swirling within a turbulent flow have been shown to be structured in worms [27,41,42] with a typical diameter on the order of 5η–10η and possibly an axial length of up to several Taylor microscales in length [43]. These observations over the scaling of the diameter of the coherent structures of vorticity were confirmed at much larger Reynolds numbers in a recent experimental study [44] and in DNS simulations of homogeneous isotropic turbulence [29].

The scale dependence of the alignment between $\boldsymbol{\omega}$ and the eigenvectors of s_{ij} and the importance of strong local swirling are explored in Fig. 4. The figure illustrates PDFs of the magnitude of the alignment cosine between local $\boldsymbol{\omega}$, computed from the unfiltered velocity, and the eigenvectors of $\tilde{s}_{ij}$, computed from filtered fields. Figures 4(a) and 4(b) are computed from $\tilde{s}_{ij}$ in which the filter width $\Lambda = \lambda$ and Figs. 4(c) and 4(d) are computed from $\tilde{s}_{ij}$ for which $\Lambda = 3\lambda$. The data used to produce Figs. 4(a) and 4(c) is unconditioned, whereas only regions of extremely strong swirling, $\lambda_{ci} \geqslant 3.5\langle\lambda_{ci}\rangle$, where $\langle\lambda_{ci}\rangle$ is the root-mean-square swirling strength defined over locally swirling regions ($\lambda_{ci} > 0$), are used to produce the PDFs of Figs. 4(b) and 4(d). Figures 4(b) and 4(d) are thus produced from data within the worms of high local swirling.

The PDFs confirm the results of Hamlington *et al.* [26] and Leung *et al.* [30] that the local (unfiltered, small-scale) vorticity preferentially aligns with the most extensive large-scale strain-rate eigenvector, in contrast to the global picture of Fig. 1 in which it is preferentially aligned with the small-scale intermediate eigenvector. However, the above PDFs show that this alignment tendency falls as Λ is increased from λ to 3λ. We may quantify the probability of parallel alignment between $\boldsymbol{e}_1$ computed from $\tilde{s}_{ij}$ defined by filter length Λ as

$$P_{\parallel}(\Lambda) = \int_{\mathcal{T}}^{1} \mathcal{F}(|\boldsymbol{e}_1 \cdot \hat{\boldsymbol{\omega}}|, \Lambda) d|\boldsymbol{e}_1 \cdot \hat{\boldsymbol{\omega}}|,$$

where $\mathcal{T}$ is some arbitrarily chosen threshold. We take $\mathcal{T} = 0.965$, which corresponds to $|\theta| = 15^\circ$, where θ is the angle between $\boldsymbol{e}_1$ and $\hat{\boldsymbol{\omega}}$, and compute the ratio $P_{\parallel}(\lambda)/P_{\parallel}(3\lambda) = 1.36$, with $P_{\parallel}(\lambda) = 0.069$. The current simulation has a spatial resolution of 2.5η and ratio $\lambda/\eta \approx 30$ and thus the ratio of strain-rate length scale to vorticity length scale, which we denote by R_Λ, is approximately 12 and 36 for $\Lambda = \lambda$ and $\Lambda = 3\lambda$, respectively. Although the definition that we take for parallel alignment, namely, the value of $\mathcal{T}$, differs from that of Leung *et al.* [30], as does the turbulent Reynolds number Re_λ and filter definitions, their ratio $P_{\parallel}(R_\Lambda = 10)/P_{\parallel}(R_\Lambda = 30) \approx 2$ is of the same order of magnitude as, but greater than, the value that we compute above. The data of Leung *et al.* [30] are from decaying homogeneous isotropic turbulence, which is a significantly different flow with respect to the mixing layer analyzed in the present work.

The figure further shows that the alignment tendencies of $\boldsymbol{\omega}$ with $\boldsymbol{e}_1$ computed from $\tilde{s}_{ij}$ (large-scale strain field) are enhanced when only the intensely swirling regions are concerned. For example, $P_{\parallel}(\lambda) = 0.13$ when only the strongly swirling regions are concerned, which is almost double that for the global data set. This increased tendency for parallel alignment between the two vectors in the strongly swirling regions perhaps may explain the collocation of regions of high $\omega_i s_{ij} \omega_j$ and strong swirling [24].

Of further interest it can be seen that, regardless of the definition of Λ or whether only the strongly swirling regions of the flow are considered or not, the PDF for $|\boldsymbol{e}_2 \cdot \hat{\boldsymbol{\omega}}|$ is nearly flat, indicating an arbitrary alignment between the two vectors. Additionally, the PDF of $|\boldsymbol{e}_3 \cdot \hat{\boldsymbol{\omega}}|$ is also only weakly dependent on Λ and λ_{ci} and displays the same quantitative trend as that in Fig. 1, in which perpendicular alignment between the two vectors is preferred. We may thus conclude that the interaction between strain rate and rotation is dictated by the extensional and intermediate strain rates only. The preferentially perpendicular alignment between the compressive strain rate and the vorticity vector appears to be universal regardless of whether the strain-rate is local or nonlocal and whether we consider regions of intense swirling or the background sea within a turbulent flow.

Figure 5 shows the PDFs of the magnitude of the alignment cosines between the filtered vorticity vector $\tilde{\boldsymbol{\omega}}$ and the eigenvectors of the filtered strain-rate tensor $\tilde{s}_{ij}$. Both vectors are thus computed from the identically filtered velocity field. Figures 5(a), 5(c), and 5(e) are computed from all regions for which the local swirling strength is defined, i.e., $\lambda_{ci} > 0$, and Figs. 5(b), 5(d), and 5(f) are computed from only the intensely swirling regions, in which $\lambda_{ci} > 3.5\langle\lambda_{ci}\rangle$ from the unfiltered velocity vector fields. Here Λ is increased from Figs. 5(a) and 5(b) ($\Lambda = \lambda$) to Figs. 5(c) and 5(d) ($\Lambda = 2\lambda$) to Figs. 5(e) and 5(f) ($\Lambda = 3\lambda$).

The PDFs of Figs. 5(a), 5(c), and 5(e) all show the same qualitative behavior as Fig. 1, with a preferential parallel alignment between $\boldsymbol{\omega}$ and $\boldsymbol{e}_2$, perpendicular alignment between $\boldsymbol{\omega}$ and $\boldsymbol{e}_3$, and arbitrary alignment between $\boldsymbol{\omega}$ and $\boldsymbol{e}_1$ [with the exception of Fig. 5(a)]. This suggests a scale independence of the qualitative behavior, at least, of the global alignment preferences between rotation and strain rate, making the enforcement of such alignment tendencies a potentially attractive SGS model for large-eddy simulations. These tendencies become more pronounced as we increase the size of Λ up to 3λ. It is thus apparent that the tendency for the vorticity vector to align in parallel with its local induced strain field increases as we consider ever larger scales (filter lengths). We again observe that the qualitative and quantitative behavior of the PDF of $|\boldsymbol{e}_3 \cdot \hat{\boldsymbol{\omega}}|$ is remarkably similar,

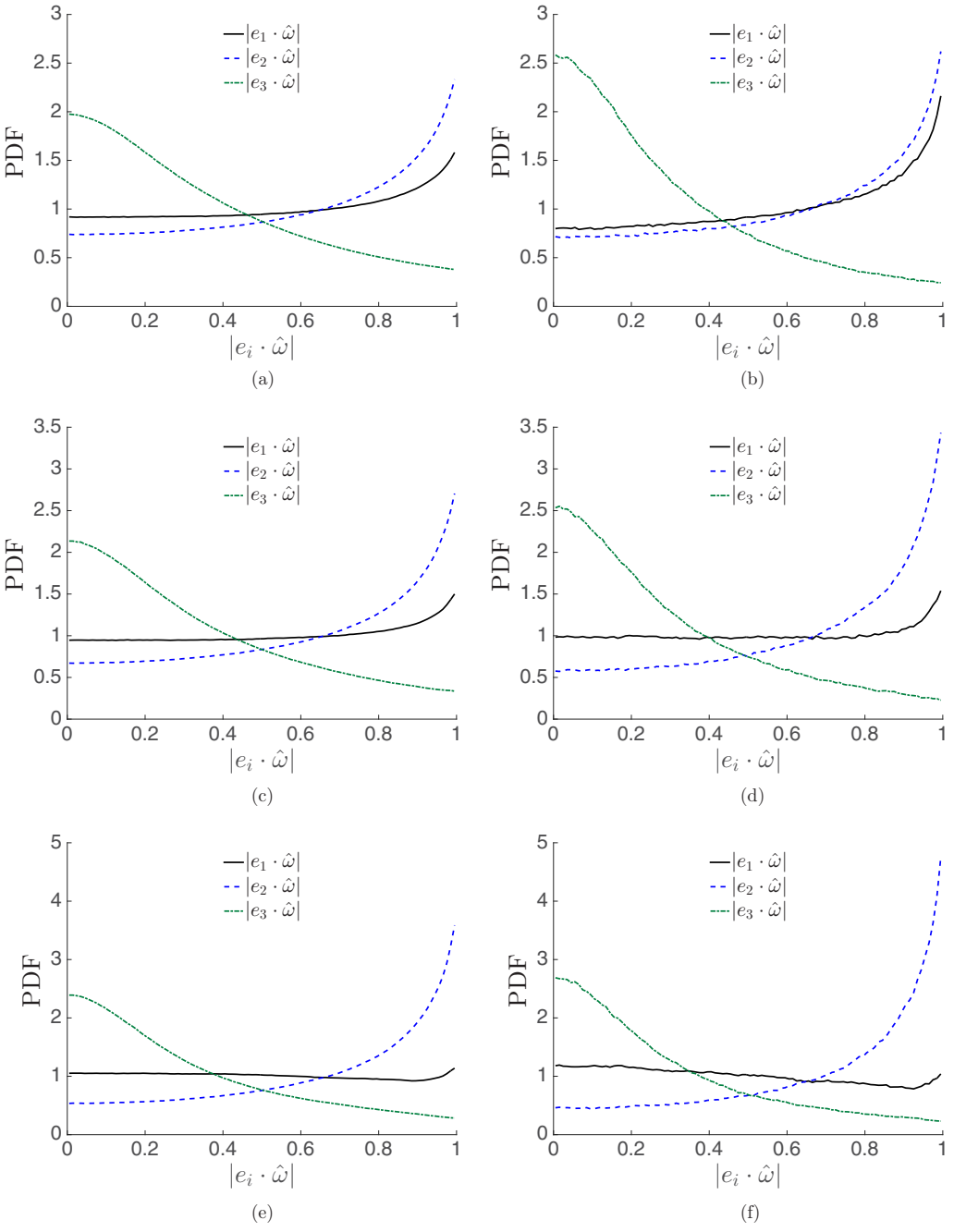

FIG. 5. Probability density functions of the alignment between the filtered vorticity vector and the eigenframe of the filtered strain-rate tensor. Both the vorticity vector and strain-rate tensor are computed from the filtered velocity field with filter length scale (a) and (b) $\Lambda = \lambda$, (c) and (d) $\Lambda = 2\lambda$, and (e) and (f) $\Lambda = 3\lambda$. Data are included only from only regions with (a), (c), and (e) a nonzero swirling strength λ_{ci} and (b), (d), and (f) intense swirling $\lambda_{ci} > 3.5\langle\lambda_{ci}\rangle$.

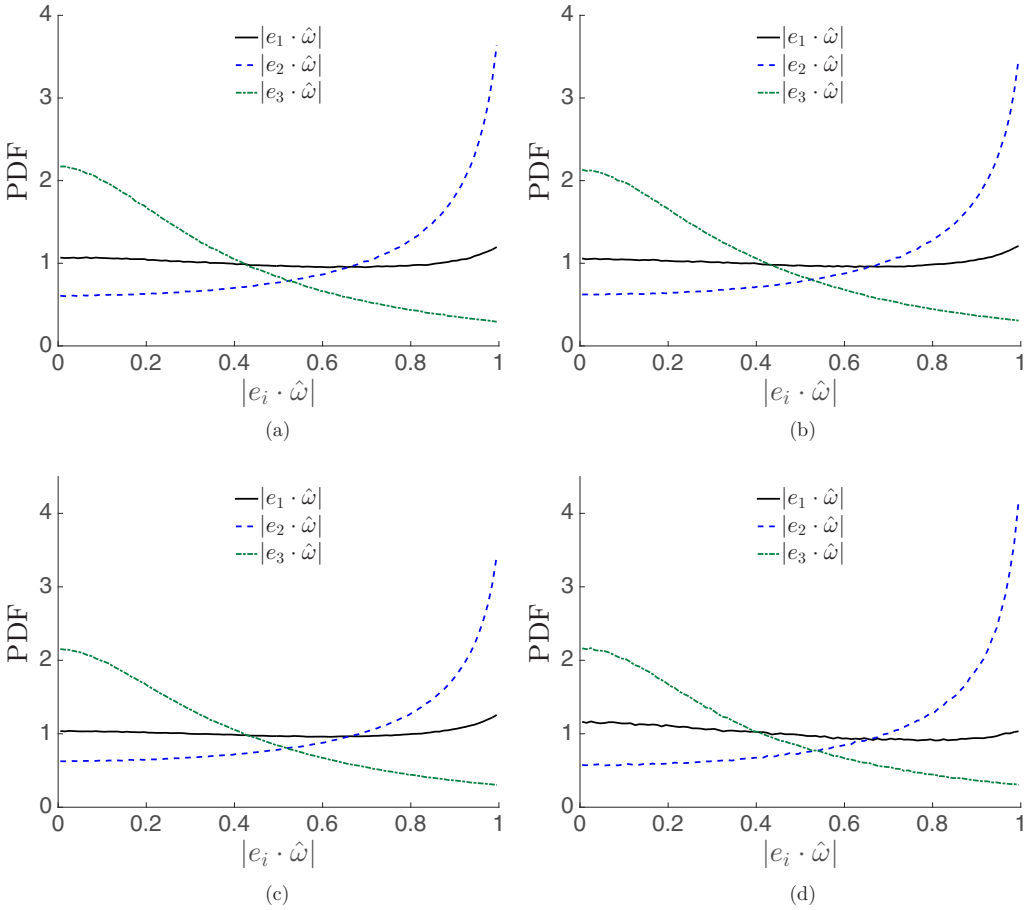

FIG. 6. Probability density functions of the magnitude of the alignment cosines between the unfiltered strain-rate eigenvectors and vorticity vector conditioned on (a) $u_L^* < 0.1$, (b) $u_L^* > 0.1$, (c) $g_L^* < 1$, and (d) $g_L^* > 1.5$.

regardless of our definition of Λ or whether we consider only the intense swirling regions or not [Figs. 5(b), 5(d), and 5(f)].

The behavior of the alignment tendencies when only the intensely swirling regions are considered is presented in Figs. 5(b), 5(d), and 5(f). The scale independence of the $|\boldsymbol{e}_3 \cdot \hat{\boldsymbol{\omega}}|$ PDF is again evident, with virtually identical quantitative behavior for all three figures. However, there is a significant scale dependence on both the $|\boldsymbol{e}_2 \cdot \hat{\boldsymbol{\omega}}|$ alignment and to a lesser extent the $|\boldsymbol{e}_1 \cdot \hat{\boldsymbol{\omega}}|$ alignment. The peak at $|\boldsymbol{e}_2 \cdot \hat{\boldsymbol{\omega}}| \approx 1$ increases in magnitude as Λ is increased from λ to 3λ. There is a slight, but consistent, trend for the PDF of $|\boldsymbol{e}_1 \cdot \hat{\boldsymbol{\omega}}|$ to flatten as Λ is increased from λ to 3λ. The qualitative trends for all the alignment PDFs only computed from within the high-enstrophy worms are thus exaggerated in comparison to the PDFs computed from all swirling data.

Figure 6 shows PDFs of the magnitudes of the alignment cosines between $\boldsymbol{\omega}$ and the eigenvectors of s_{ij}, both computed from the unfiltered velocity field and conditioned on concurrent, high-magnitude large-scale fluctuations. Figures 6(a) and 6(b) show these PDFs conditioned on the sign of the large-scale velocity fluctuations $u_L^* < 0.1$ and $u_L^* > 0.1$, respectively. Figures 6(c) and 6(d) are the PDFs conditioned on the magnitude of the large-scale velocity gradients $g_L^* < 1$ and $g_L^* > 1.5$, respectively, where g_L^* has been defined in Sec. III.

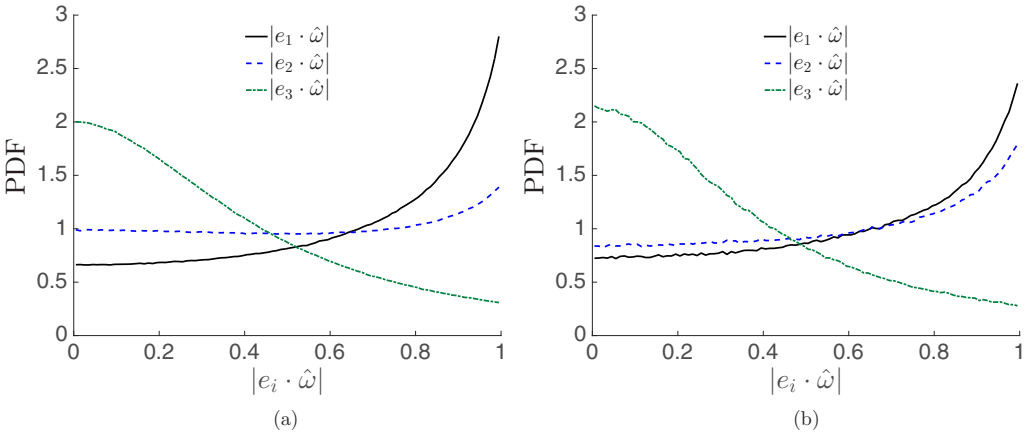

FIG. 7. Probability density functions of the alignment between the filtered eigenframe of the strain-rate tensor ($\Lambda = \lambda$) and the unfiltered vorticity vector conditioned on (a) $g_L^* < 1$ and (b) $g_L^* > 1.5$.

It can be seen that there are no large qualitative differences between the PDFs in the four figures, with the general picture being the same as that in Fig. 1, the unconditioned case. In particular it can again be seen that the PDF of $|\boldsymbol{e}_3 \cdot \hat{\boldsymbol{\omega}}|$ remains virtually constant despite the condition of the large-scale fluctuation, whether that be u_L^* or g_L^*. The primary quantitative difference is that between Figs. 6(c) and 6(d), the PDFs of $|\boldsymbol{e}_1 \cdot \hat{\boldsymbol{\omega}}|$ and $|\boldsymbol{e}_2 \cdot \hat{\boldsymbol{\omega}}|$ conditioned on $g_L^* < 1$ and $g_L^* > 1.5$, respectively. If we now consider the probability of parallel alignment between $\boldsymbol{e}_2$ and $\boldsymbol{\omega}$ in a similar fashion to before,

$$P_{\parallel}(g_L^*) = \int_{\mathcal{T}}^{1} \mathcal{F}(|\boldsymbol{e}_2 \cdot \hat{\boldsymbol{\omega}}|, g_L^*) d|\boldsymbol{e}_2 \cdot \hat{\boldsymbol{\omega}}|,$$

again using $\mathcal{T} = 0.965$, we obtain $P_{\parallel}(g_L^* < 1) = 0.088$ and $P_{\parallel}(g_L^* > 1.5) = 0.103$. This effect is important and it lends credence to the argument of Fiscaletti *et al.* [14] that concurrent fluctuations in the large-scale velocity gradient drive the scale interactions with the small-scale velocity gradient phenomena. It is thus clear that the scale interaction by which the concurrent large-scale velocity fluctuation affects the small-scale $\omega_i s_{ij} \omega_j$ reported by Buxton [12] is likely not driven by an alteration in the alignment tendencies between $\boldsymbol{\omega}$ and $\boldsymbol{e}_i$ and is instead more likely due to a modulation of the magnitudes of ω^2 and s_i (the strain-rate eigenvalues) or their correlations with $|\boldsymbol{e}_i \cdot \hat{\boldsymbol{\omega}}|$. In particular, the relation between ω^2 and the large-scale velocity fluctuations simply denotes a spatial inhomogeneous distribution of the regions characterized by large ω^2 across the mixing layer, as shown by Fiscaletti *et al.* [14]. Instead, an active small-scale modulation is exerted by $\tilde{s}_{ij}$ or, similarly, by the large-scale gradients g_L^*. Evidence for this is given by the correlation coefficient between the large-scale gradients and the small-scale enstrophy being close to unity throughout the mixing layer [14].

Figure 7 shows the PDFs of the magnitude of the alignment cosines between $\boldsymbol{\omega}$ and the eigenvectors of $\tilde{s}_{ij}$, with a filter length scale $\Lambda = \lambda$, conditioned on the concurrent large-scale velocity gradients. It is again evident that the quantitative behaviors of the PDFs of $|\boldsymbol{e}_3 \cdot \hat{\boldsymbol{\omega}}|$ are virtually identical, regardless of the nature of the concurrent large-scale velocity gradients, with a similar behavior to the unconditioned PDF of Fig. 1. We again observe the behavior reported by Hamlington *et al.* [26] and Leung *et al.* [30] that the vorticity vector preferentially aligns in parallel with the filtered (background) extensive strain-rate eigenvector. However, we observe a slight decrease in the peak value of the PDF for $|\boldsymbol{e}_1 \cdot \hat{\boldsymbol{\omega}}| \approx 1$ and a corresponding increase in the tendency for $\boldsymbol{\omega}$ to be aligned in parallel with $\boldsymbol{e}_2$ when the magnitude of the concurrent large-scale velocity gradient is large. This indicates a tendency for the vorticity vector to be better self-aligned, i.e., aligned to the strain

field that is produced locally, in regions of the flow for which the large-scale velocity gradient is large. According to Fiscaletti *et al.* [14], the correlation coefficients between the large-scale velocity gradients and the rms vorticity is close to unity throughout the mixing layer. This implies that large values of the large-scale velocity gradients induce locally a larger rms vorticity, therefore a larger ω^2. The shear induced by the local amplification of ω^2 affects the filtered strain field, especially for a filter size of $\Lambda = \lambda$. As a consequence, the vorticity vector tends to be more aligned with the intermediate eigenvector of the strain-rate tensor.

V. CONCLUSION

The scale dependence of the alignment between the vorticity vector and the eigenvectors of the strain-rate tensor was examined in the self-preserving region of a turbulent shear flow. It was observed that these alignment tendencies were largely unaltered when conditioned on the sign of the concurrent large-scale velocity fluctuations, but were affected when conditioned on the magnitude of the concurrent large-scale velocity-gradient fluctuations. This observation adds weight to the argument of Fiscaletti *et al.* [14], who suggested that the concurrent large-scale velocity gradients play the largest role in affecting the energy content of the small scales.

The results of Hamlington *et al.* [26] and Leung *et al.* [30] for homogeneous isotropic turbulence were confirmed in the present free-shear flow, namely, that the local (small-scale) vorticity vector preferentially aligns in parallel with the nonlocal (large-scale) extensive strain-rate eigenvector. By virtue of the fact that the corresponding extensive strain-rate eigenvalue is the largest in magnitude, a positive strain rate makes this alignment the most significant contribution to $\langle \omega_i s_{ij} \omega_j \rangle$ [30], the positivity of which is responsible for the net cascade of energy from large scales to small scales. The probability of parallel alignment, arbitrarily defined in this paper by $|\theta| < 15^\circ$, is significantly enhanced when only data from the strongly swirling worms are considered. This finding provides further evidence for the collocation of regions of intense enstrophy amplification ($\omega_i s_{ij} \omega_j \gg 0$) with these intensely swirling worms [24]. The tendency for parallel alignment was also observed to decrease as the definition of the nonlocal strain-rate field was narrowed to include increasingly large scales only. This is in agreement with Leung *et al.* [30], however the ratio of this decline was significantly different, which can be explained by a flow and Reynolds-number dependence on this tendency.

When both the vorticity vector and the strain-rate tensor are obtained from a filtered velocity field it is observed that the alignment statistics between $\boldsymbol{\omega}$ and the eigenvectors of $\tilde{s}_{ij}$ do not vary in response to changing the length scale of the filter (or in the absence of filtering). This scale-independent behavior thus makes the enforcement of this canonical alignment behavior an interesting proposition for the development of SGS models for large-eddy simulations. The most scale independent of the alignment tendencies is that between $\boldsymbol{\omega}$ and $\boldsymbol{e}_3$, the compressive strain-rate eigenvector. Regardless of the filter size and whether only swirling regions are considered or not, the qualitative behavior of the $|\boldsymbol{e}_3 \cdot \hat{\boldsymbol{\omega}}|$ PDF remains similar, with only marginal quantitative differences. Further investigations on different flows at different Reynolds numbers are required in order to consider these observations a universal feature of turbulent flows.

ACKNOWLEDGMENTS

We acknowledge valuable support from KAUST Supercomputing Laboratory in the form of assistance with code development and computational time on the IBM System Blue Gene/P "Shaheen" at King Abdullah University of Science and Technology.

[1] L. F. Richardson, Atmospheric diffusion shown on a distance-neighbour graph, Proc. R. Soc. London Ser. A **110**, 709 (1926).

[2] A. N. Kolmogorov, The local structure of turbulence in incompressible viscous fluid for very large Reynolds numbers, Dokl. Akad. Nauk SSSR **30**, 301 (1941).
[3] U. Piomelli *et al.*, Subgrid-scale backscatter in turbulent and transitional flows, Phys. Fluids A **3**, 1766 (1991).
[4] A. N. Kolmogorov, A refinement of previous hypotheses concerning the local structure of turbulence in a viscous incompressible fluid at high Reynolds number, J. Fluid Mech. **13**, 82 (1962).
[5] S. B. Pope, *Turbulent Flows* (Cambridge University Press, Cambridge, 2000).
[6] G. K. Batchelor and A. A. Townsend, The nature of turbulent motion at large wave-numbers, Proc. R. Soc. London Ser. A **199**, 238 (1949).
[7] P. K. Yeung, J. G. Brasseur, and Q. Wang, Dynamics of direct large-small scale couplings in coherently forced turbulence: Concurrent physical- and Fourier-space views, J. Fluid Mech. **283**, 43 (1995).
[8] X. Shen and Z. Warhaft, The anisotropy of the small scale structure in high Reynolds number ($R_\lambda \sim 1000$) turbulent shear flow, Phys. Fluids **12**, 2976 (2000).
[9] P. R. Bandyopadhyay and K. M. F. Hussain, The coupling between scales in shear flows, Phys. Fluids **27**, 2221 (1984).
[10] C. Meneveau, Statistics of turbulence subgrid-scale stresses: Necessary conditions and experimental tests, Phys. Fluids **6**, 815 (1994).
[11] O. R. H. Buxton and B. Ganapathisubramani, Concurrent scale interactions in the far-field of a turbulent mixing layer, Phys. Fluids **26**, 125106 (2014).
[12] O. R. H. Buxton, Modulation of the velocity gradient tensor by concurrent large-scale velocity fluctuations in a turbulent mixing layer, J. Fluid Mech. **777**, R1 (2015).
[13] J. O'Neil and C. Meneveau, Subgrid-scale stresses and their modeling in a turbulent plane wake, J. Fluid Mech. **349**, 253 (1997).
[14] D. Fiscaletti *et al.*, Scale interactions in a mixing layer—The role of the large-scale gradients, J. Fluid Mech. **791**, 154 (2016).
[15] G. I. Taylor, Production and dissipation of vorticity in a turbulent fluid, Proc. R. Soc. London Ser. A **164**, 15 (1938).
[16] R. J. Betchov, An inequality concerning the production of vorticity in isotropic turbulence, J. Fluid Mech. **1**, 497 (1956).
[17] G. E. Elsinga and I. Marusic, Universal aspects of small-scale motions in turbulence, J. Fluid Mech. **662**, 514 (2010).
[18] G. E. Elsinga and I. Marusic, The anisotropic structure of turbulence and its energy spectrum, Phys. Fluids **28**, 011701 (2016)
[19] W. T. Ashurst *et al.*, Alignment of vorticity and scalar gradient with strain rate in simulated Navier-Stokes turbulence, Phys. Fluids **30**, 2343 (1987).
[20] Z. S. She, E. Jackson, and S. A. Orszag, Structure and dynamics of homogeneous turbulence: Models and simulation, Proc. R. Soc. London A **434**, 101 (1991).
[21] A. Tsinober, E. Kit, and T. Dracos, Experimental investigation of the field of velocity gradients in turbulent flows, J. Fluid Mech. **242**, 169 (1992).
[22] A. Vincent and M. Meneguzzi, The dynamics of vorticity tubes in homogeneous turbulence, J. Fluid Mech. **258**, 245 (1994).
[23] A. Attili and F. Bisetti, Statistics and scaling of turbulence in a spatially developing mixing layer at $\mathrm{Re}_\lambda = 250$, Phys. Fluids **24**, 035109 (2012).
[24] O. R. H. Buxton and B. Ganapathisubramani, Amplification of enstrophy in the far field of an axisymmetric turbulent jet, J. Fluid Mech. **651**, 483 (2010).
[25] K. N. Nomura and G. K. Post, The structure and dynamics of vorticity and rate of strain in incompressible homogeneous turbulence, J. Fluid Mech. **377**, 65 (1998).
[26] P. E. Hamlington, J. Schumacher, and W. J. A. Dahm, Direct assessment of vorticity alignment with local and nonlocal strain rates in turbulent flows, Phys. Fluids **20**, 111703 (2008).
[27] J. Jiménez, A. A. Wray, P. G. Saffman, and R. S. Rogallo, The structure of intense vorticity in isotropic turbulence, J. Fluid Mech. **255**, 65 (1993).

[28] S. Herpin *et al.*, Influence of the Reynolds number on the vortical structures in the logarithmic region of turbulent boundary layers, J. Fluid Mech. **716**, 5 (2013).
[29] T. Ishihara, Y. Kaneda, and J. C. R. Hunt, Thin shear layers in high Reynolds number turbulence—DNS results, Flow Turbul. Combust. **91**, 895 (2013).
[30] T. Leung, N. Swaminathan, and P. A. Davidson, Geometry and interaction of structures in homogeneous isotropic turbulence, J. Fluid Mech. **710**, 453 (2012).
[31] O. Desjardins *et al.*, High order conservative finite difference scheme for variable density low Mach number turbulent flows, J. Comput. Phys. **227**, 7125 (2008).
[32] A. Attili *et al.*, Effects of non-unity Lewis number of gas-phase species in turbulent nonpremixed sooting flames, Combust. Flame **166**, 192 (2016).
[33] A. Attili and F. Bisetti, Fluctuations of a passive scalar in a turbulent mixing layer, Phys. Rev. E **88**, 033013 (2013).
[34] A. Attili, J. C. Cristancho, and F. Bisetti, Statistics of the turbulent/non-turbulent interface in a spatially developing mixing layer, J. Turbul. **15**, 555 (2014).
[35] J. Kim and P. Moin, Application of a fractional-step method to incompressible Navier-Stokes equations, J. Comput. Phys. **59**, 308 (1985).
[36] M. A. Ol'Shanskii and V. M. Staroverov, On simulation of outflow boundary conditions in finite difference calculations for incompressible fluid, Int. J. Numer. Meth. Fluids **33**, 499 (2000).
[37] C. Pantano and S. Sarkar, A study of compressibility effects in the high-speed turbulent shear layer using direct simulation, J. Fluid Mech. **451**, 329 (2002).
[38] G. I. Taylor, Statistical theory of turbulence, Proc. R. Soc. London Ser. A **151**, 421 (1935).
[39] G. I. Taylor, The spectrum of turbulence, Proc. R. Soc. London Ser. A **164**, 476 (1938).
[40] J. Zhou *et al.*, Mechanisms for generating coherent packets of hairpin vortices in channel flow, J. Fluid Mech. **387**, 353 (1999).
[41] E. D. Siggia, Numerical study of small-scale intermittency in three dimensional turbulence, J. Fluid Mech. **107**, 375 (1981).
[42] R. M. Kerr, Higher-order derivative conclusions and the alignment of small-scale structures in isotropic numerical turbulence, J. Fluid Mech. **153**, 31 (1985).
[43] B. Ganapathisubramani, K. Lakshminarasimhan, and N. T. Clemens, Investigation of three-dimensional structure of fine scales in a turbulent jet by using cinematographic stereoscopic particle image velocimetry, J. Fluid Mech. **598**, 141 (2008).
[44] D. Fiscaletti, J. Westerweel, and G. E. Elsinga, Long-range μPIV to resolve the small scales in a jet at high Reynolds number, Exp. Fluids **55**, 1812 (2014).